DRAFT VERSION DECEMBER 22, 2021
Preprint typeset using LaTeX style emulateapj v. 5/2/11

arXiv:1512.04447v1 [astro-ph.SR] 14 Dec 2015

TRANSITION REGION ABUNDANCE MEASUREMENTS DURING IMPULSIVE HEATING EVENTS

HARRY P. WARREN[1], DAVID H. BROOKS[2,3], GEORGE A. DOSCHEK[1], URI FELDMAN[4]
[1]Space Science Division, Naval Research Laboratory, Washington, DC 20375 USA
[2]College of Science, George Mason University, 4400 University Drive, Fairfax, VA 22030 USA and
[4]Artep, Inc., 2922 Excelsior Springs Court, Ellicott City, MD 21042, USA
Draft version December 22, 2021

ABSTRACT

It is well established that elemental abundances vary in the solar atmosphere and that this variation is organized by first ionization potential (FIP). Previous studies have shown that in the solar corona low-FIP elements, such as Fe, Si, Mg, and Ca, are generally enriched relative to high-FIP elements, such as C, N, O, Ar, and Ne. In this paper we report on measurements of plasma composition made during impulsive heating events observed at transition region temperatures with the Extreme Ultraviolet Imaging Spectrometer (EIS) on *Hinode*. During these events the intensities of O IV, V, and VI emission lines are enhanced relative to emission lines from Mg V, VI, and VII and Si VI and VII and indicate a composition close to that of the photosphere. Long-lived coronal fan structures, in contrast, show an enrichment of low-FIP elements. We conjecture that the plasma composition is an important signature of the coronal heating process, with impulsive heating leading to the evaporation of unfractionated material from the lower layers of the solar atmosphere and higher frequency heating leading to long-lived structures and the accumulation of low-FIP elements in the corona.

Subject headings: Sun: magnetic fields

1. INTRODUCTION

Understanding how mass and energy flows through the solar upper atmosphere is one of the most complex problems in astrophysics. One important clue to understanding this process lies in the fact that the plasma composition is not constant throughout the solar atmosphere, but varies from feature to feature. These variations are organized by first ionization potential (FIP), elements with a FIP below 10 eV, such as Fe, Si, Mg, and Ca, are generally enriched in the solar corona, while elements with higher FIP, such as C, N, O, Ar, and Ne, have the composition of the photosphere (for a review of measurements and models see Laming 2015). The fact that this behavior depends on the first ionization potential suggests that the fractionation occurs in the solar chromosphere, where the high-FIP elements are neutral and the low-FIP elements are ionized.

Observations of high temperature, active region plasma indicate an enrichment of 3–4 for low-FIP elements. For example, Del Zanna & Mason (2014), reanalyzed soft X-ray observations from the Solar Maximum Mission (SMM) and found an enrichment of about 3.2 in non-flaring active regions. Del Zanna (2013b) derived a similar value for the enrichment of low-FIP elements in active region emission using observations from the Extreme Ultraviolet Imaging Spectrometer (EIS) on *Hinode*. Warren et al. (2012) used EIS observations to measure the temperature structure of 15 active regions and found the relative intensities of high-FIP lines to be consistent with a coronal composition. Furthermore, these analyses found relatively narrow temperature distributions in the core of the active region near 3–4 MK.

Recent measurements in solar flares have generally indicated abundances that are much closer to that of the photosphere. Dennis et al. (2015), Fludra & Schmelz (1999), and Warren (2014), for example, found enrichments of 1.66 ± 0.34, 1.4 ± 0.4, 1.17 ± 0.22, respectively, of high temperature Fe lines observed in a large sample of solar flares. Sylwester et al. (2015) derived abundances close to photospheric for high temperature Si, Ar, and S lines observed during flares. In many of these studies the temperature distributions are observed to be very broad with a peak near 10 MK.

The differences in composition and temperature distribution between high temperature active region plasma and high temperature solar flare plasma suggest that they may be heated in different ways. One possible scenario is that active region loops are heated by frequent, small scale events that keep these loops relatively close to equilibrium. Individual flare loops, in contrast, could be heated impulsively and are always evolving. This would account for the differences in temperature distributions (narrow vs. broad) and the composition (coronal vs. photospheric), since it appears that the fractionation process takes several days to enrich the corona with low-FIP elements (e.g., Sheeley 1995; Widing & Feldman 2001).

Unfortunately, not all of the observational evidence is consistent with this simple picture. Dennis et al. (2015) and Doschek et al. (2015), for example, find that Ca is enriched at all times during flares. Sylwester et al. (2015) find evidence for a similar enrichment in K emission. Doschek et al. (2015) have even identified isolated regions in several flares where Ar emission is strongly enhanced relative to Ca.

It is clear that additional observations are needed to make progress on understanding the relationship between plasma composition and the coronal heating process. It has long been recognized that the transition region, the interface between the hot corona and the mass reservoir of the chromosphere, should provide important information. The complexity of the solar transition region emission and the high cadence, high spatial resolution, and broad wavelength coverage needed to observe it, however, have largely thwarted this approach.

In this paper we present the analysis of transition region emission observed with the EIS spectrometer on *Hinode*. At the EUV wavelengths observed by EIS, the transition region emission lines are weak. They can, however, be observed easily during intense heating events such as flares. We find that

[3] Present address: Hinode Team, ISAS/JAXA, 3-1-1 Yoshinodai, Chuo-ku, Sagamihara, Kanagawa 252-5210, Japan

TABLE 1
EIS EMISSION LINES OF INTEREST[a]

Line	$\log T_*$	$\log n_*$	$\epsilon(T_*, n_*)$	FIP	A_p	A_c
O IV 279.933	5.26	10.44	1.45e-25	13.6	8.76	8.76
O V 248.456	5.42	10.28	1.90e-25	13.6	8.76	8.76
Mg V 276.579	5.50	10.20	5.13e-26	7.6	7.54	8.14
O VI 184.117	5.52	10.18	5.90e-26	13.6	8.76	8.76
Si VI 246.004	5.64	10.06	5.44e-26	8.2	7.52	8.12
Mg VI 268.986	5.66	10.04	2.32e-26	7.6	7.54	8.14
Mg VII 276.153	5.80	9.90	1.15e-26	7.6	7.54	8.14
Mg VII 280.737	5.78	9.92	4.02e-26	7.6	7.54	8.14
Si VII 275.368	5.80	9.90	8.06e-26	8.2	7.52	8.12
Fe IX 197.862	5.96	9.74	1.98e-26	7.9	7.52	8.12
Fe X 184.536	6.06	9.64	1.06e-25	7.9	7.52	8.12
Fe XI 180.401	6.14	9.56	3.29e-25	7.9	7.52	8.12
Si X 258.375	6.14	9.56	9.92e-26	8.2	7.52	8.12
S X 264.233	6.18	9.52	3.33e-26	10.4	7.16	7.16
Fe XII 192.394	6.20	9.50	8.08e-26	7.9	7.52	8.12
Fe XIII 202.044	6.26	9.44	9.16e-26	7.9	7.52	8.12
Fe XIII 203.826	6.24	9.46	2.09e-25	7.9	7.52	8.12
Fe XIV 274.203	6.30	9.40	9.75e-26	7.9	7.52	8.12
Fe XV 284.160	6.34	9.36	5.55e-25	7.9	7.52	8.12
Fe XVI 262.984	6.42	9.28	2.19e-26	7.9	7.52	8.12

[a] Plasma emissivity as a function of temperature is shown in Figure 1. Here we show the peak temperature (T_*), the number density at the peak temperature (n_*), and the emissivity computed for these parameters assuming a photospheric composition. Also shown for each ion are the FIP in eV and the logarithmic abundances relative to H ($A_H = 12$). The photospheric abundances (A_p) are those tabulated by Caffau et al. (2011). For coronal abundances (A_c) we approximate the tabulation of Feldman et al. (1992) by scaling the photospheric abundances of the low FIP elements by a factor of 4 and leaving the abundances of the high FIP elements unchanged.

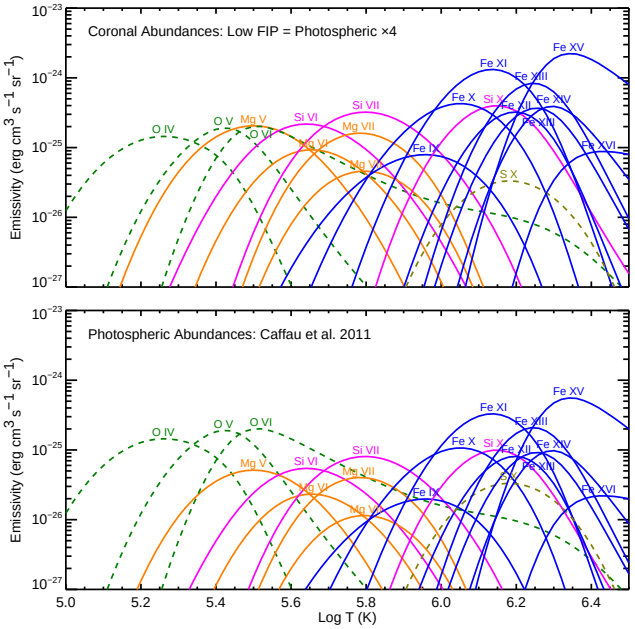


FIG. 1.— Plasma emissivity as a function of temperature for the EIS emission lines of interest. A constant pressure of 10^{16} cm^{-3} K has been assumed. Calculations are shown for photospheric and coronal abundances. Emissivities for high-FIP elements are shown with dashed lined. These calculations suggest that O V and O VI emission lines should be bright relative to Mg V, Mg VI, and Si VI when the composition is photospheric.

during these events the observed intensities are generally consistent with a plasma composition close to that of the photosphere. For long-lived coronal "fans, " in contrast, the line intensities are more consistent with a coronal composition.

2. OBSERVATIONS

EIS (Culhane et al. 2007; Korendyke et al. 2006) is a high spatial and spectral resolution imaging spectrograph. EIS observes two wavelength ranges, 171–212 Å and 245–291 Å, with a spectral resolution of about 22 mÅ and a spatial resolution of about 1″ per pixel. Solar images can be made by stepping the slit over a region of the Sun and taking an exposure at each position.

Some information on the EIS emission lines of interest for this study is shown in Table 1 and in Figure 1. These data are taken from the CHIANTI atomic database version 8.0.1 (Del Zanna et al. 2015; Dere et al. 1997). As can be seen in the plots of plasma emissivity in Figure 1, none of the transition region emission lines that can be observed with EIS are so well matched in temperature that we can use a simple line ratio to measure the composition, as was done with the Mg VI and Ne VI lines observed with Skylab (e.g., Sheeley 1995; Widing & Feldman 2001). Instead, we will use a series of O, Mg, and Si emission lines to infer the general trends in the relative intensities between low and high-FIP elements.

In this paper we use the tabulation of Caffau et al. (2011) for the elemental abundances of the photosphere. For coronal abundances we approximate the tabulation of Feldman et al. (1992) by scaling the photospheric abundances of the low-FIP elements by a factor of 4 and leaving the abundances of the high-FIP elements unchanged. Adopting the abundances of Feldman et al. (1992) would imply changes in both the high and low-FIP elements in the corona, although the difference for the high-FIP elements would be relatively small. The relevant abundances are given in Table 1.

For the emissivities shown in Table 1 and in Figure 1 we have assumed a constant total pressure of $P = 2n_eT_e = 10^{16}\,\mathrm{cm}^{-3}$ K. To measure electron densities for our observations we use the Mg VII 280.737/276.153 (Landi & Young 2009) and Fe XIII 203.826/202.044 line ratios (Warren et al. 2010). Note that almost all of the emission lines of interest have some amount of density sensitivity so estimating the density in the emitting plasma is an important component of the analysis.

Most of the emission lines selected for this study have been analyzed extensively and are known to yield consistent results (e.g., Landi & Young 2009; Brooks et al. 2009; Warren & Brooks 2009). Unfortunately, the two O VI emission lines in the EIS wavelength range, 183.937 and 184.117 Å, are problematic. On the disk the observed 183.937/184.117 ratio differs significantly from theory. The strong wavelength shifts in the 183.937 Å line suggest that it is blended (Landi & Young 2009). The observed intensity of the longer wavelength line is not consistent with other emission lines (e.g., Warren & Brooks 2009). As can be see in Figure 1, O VI is needed to improve the overlap between the high and low-FIP transition region emission lines. For this study we scale the emissivity of O VI 184.117 Å by a factor of 3.4 in all cases. Additional details on this line and the scaling factor that we have adopted are discussed in Appendix A.

Because of telemetry constraints, EIS observations are usually structured such that a only a subset of the full detector exposures are read out and telemetered to the ground. Since we require a large number of emission lines for this analysis we will focus on the EIS ATLAS studies that record the full wavelength range over an area of $120'' \times 160''$ on the sun using the 2″ slit and 30, 60, or 120 s exposure times. These studies take between about 30 minutes and 2 hours to complete. Note

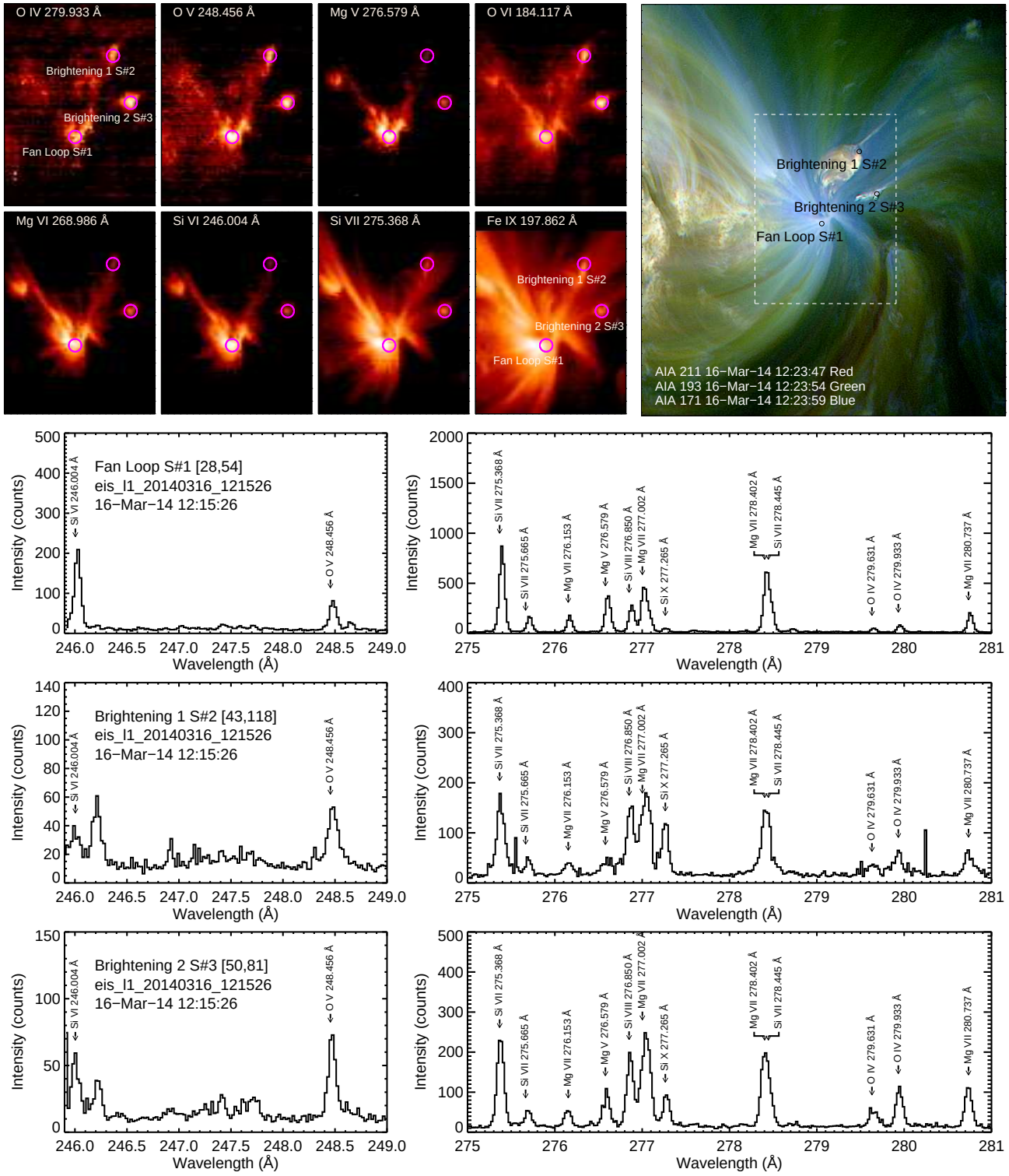


FIG. 2.— EIS and AIA observations of an active region taken on 2014 March 16 between 12:15:26 and 13:16:05 UT. The top left panels show EIS intensities in various transition region emission lines. The top right panel shows a three color AIA image taken during the EIS raster. The bottom panels show EIS spectra at selected locations. At the base of the fan loops the intensities of the low-FIP Mg and Si lines are bright relative to the high-FIP O lines, suggesting a coronal composition. In the transient brightenings the O lines are bright relative to Si and Mg, suggesting a photospheric composition.

that for these studies the slit is moved in 2″ steps across the sun.

These `Atlas` studies have been run over 500 times and to identify interesting features we created a simple summary image for each observation. The summary images contain rasters for lines formed at transition region, coronal, and flare temperatures and we manually selected observations based on the presence of strong transition region emission. Three of the selected observations were taken during flares as indicated by the presence of strong Fe XXIV 255.100 Å emission. Each ob-

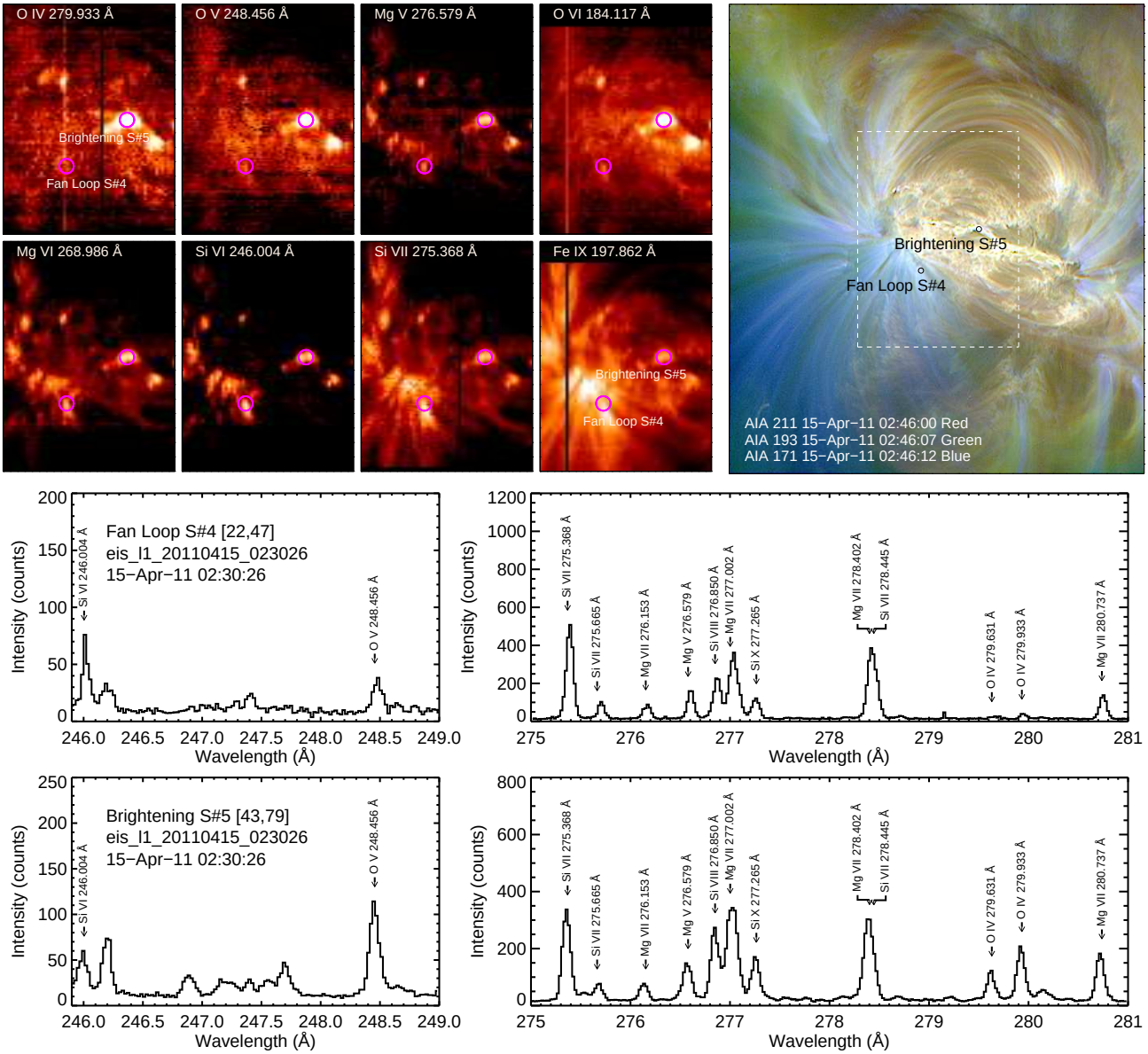


FIG. 3.— EIS and AIA observations of an active region taken on 2011 April 15 between 02:30:26 and 03:31:06 UT. The format is the same as Figure 2. In the brightening the O emission lines are bright relative to Si and Mg while in the fan loop the relative intensities are reversed.

servation is reduced in the standard way using the SSW analysis routine `eis_prep`, which removes the CCD pedestal and dark current and flags dusty and hot pixels. The data are not calibrated at this step but converted to "photon events" or counts and are calibrated at a later stage in the processing. See Freeland & Handy 1998 for a description of the Solar Software — SSW — used in the analysis of these data.

In Figures 2–7 we show EIS rasters in selected lines computed by fitting Gaussians to the line profile of interest at every spatial pixel. For each observation we also show an AIA three-color image computed by superimposing the 211 Å (red), 193 Å (green), and 171 Å channels (blue).

To co-align EIS to AIA we use a two step process to find the optimal spatial correlation between the two datasets. First we adjust the pointing provided in the EIS file headers using the results from the SSW analysis routine `eis_aia_offsets`. Second we convolve the EIS 195 Å spectral region with the AIA 193 Å effective areas and cross-correlate these intensities along the slit with the intensities in the nearest AIA 193 Å image blurred to the EIS spatial resolution. This process yields the co-alignment for each exposure. Note that for some of the flare observations either the EIS or AIA observations are saturated at some positions and the co-alignment does not work well. We exclude badly saturated exposures from consideration in this analysis.

For each observation we have selected one to three bright features in the O V 248.456 Å or Si VI 246.004 Å rasters and computed spectra as a function of wavelength for these positions. These spectra account for the spatial offset of the two EIS detectors as well as the tilt of each detector with respect to the slit. See the SSW analysis routine `eis_ccd_offset` and the corresponding documentation for additional information.

The interpolated spectrum is computed using the data in units of counts and then converted to physical units using both

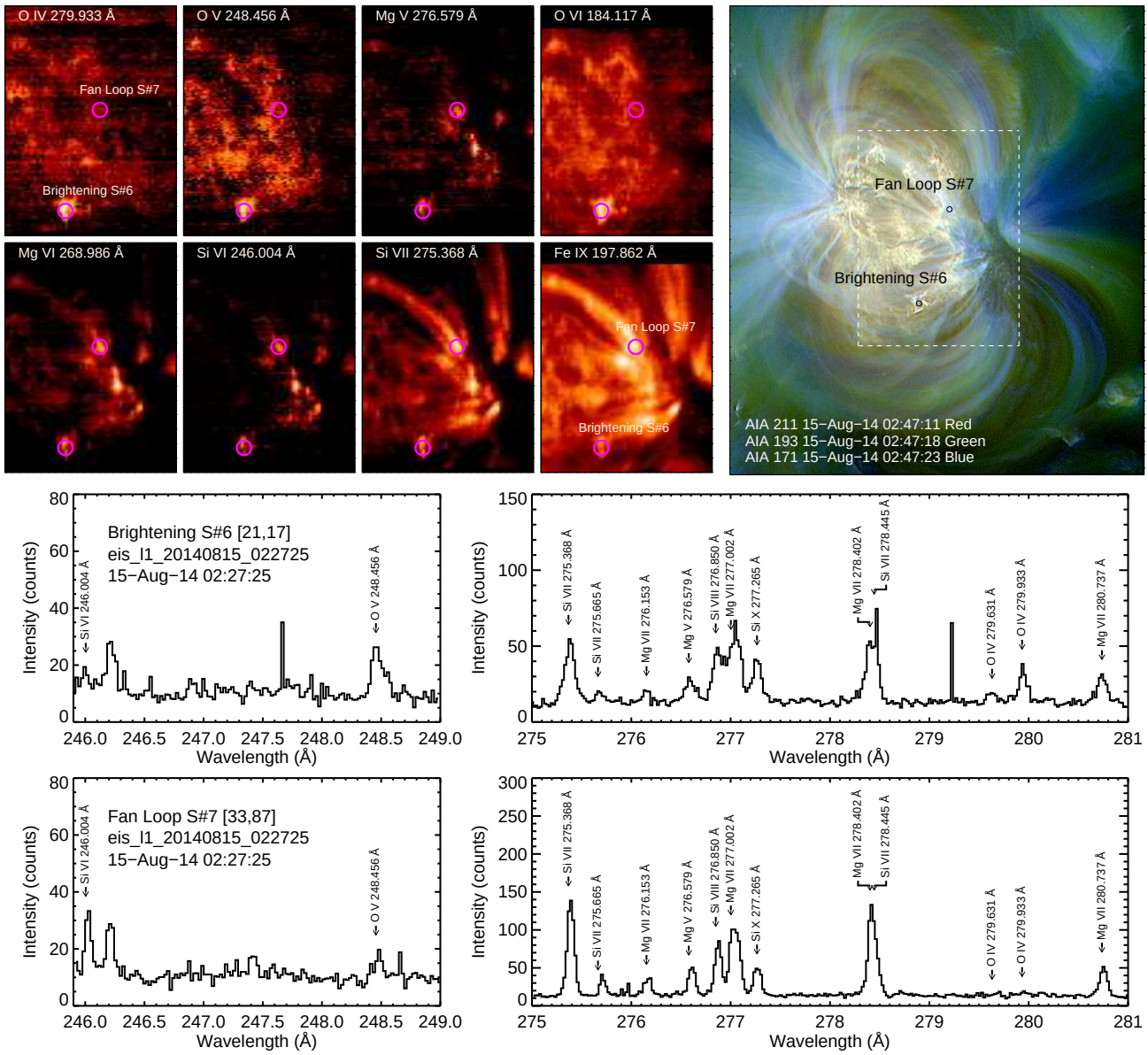


FIG. 4.— EIS and AIA observations of an active region taken on 2014 August 15 between 02:27:25 and 02:58:34 UT. The format is the same as Figure 2. Again, in the brightening the O emission lines are bright relative to Si and Mg while in the fan loop the relative intensities are reversed.

the pre-flight calibration (Lang et al. 2006) and the revised calibration of Warren et al. (2014), which includes time- and wavelength-dependent changes to the instrument sensitivity (see Del Zanna 2013a for an extensive discussion of EIS calibration issues). For this work we use the data calibrated using the Warren et al. (2014) effective areas. Additional comments on the calibration are provided in Appendix B.

Selected wavelength ranges from these spectra are shown in Figures 2–7. There are 12 spectra in total that we will consider here. Note that the dispersion for these spectra has not been optimized for velocity studies and any wavelengths shifts should be interpreted as instrumental in origin. Our primary focus here is on the interpretation of the line intensities.

We have used the co-aligned AIA observations to compute light curves for each EIS spectrum. Unsurprisingly, the bright transition region emission identified in the EIS data generally corresponds to either a transient heating event or a long, coronal "fan." The light curves for each of the transient brightenings are shown in Figure 8. The light curves for the fans, which are not shown, are remarkably constant in the AIA data.

The final step in the data reduction is to fit the emission lines of interest in each spectrum with Gaussians so that the total line intensity can be computed.

3. ANALYSIS

As mentioned previously, the low- and high-FIP emission lines observed with EIS are not so well matched in temperature that we can reduce the analysis to simple line ratios. Still, inspection of the individual spectra is revealing. For the fan loops shown in Figures 2, 3, 4, and 5, the intensity of Si VI 246.004 Å is always larger than that of the nearby O V 248.456 Å line. Similarly, Mg V 276.579 Å is always significantly more intense than the nearby O IV 279.933 Å. In the spectra from the brightenings and the flares the opposite trend is observed. For these spectra the intensity of O V 248.456 Å

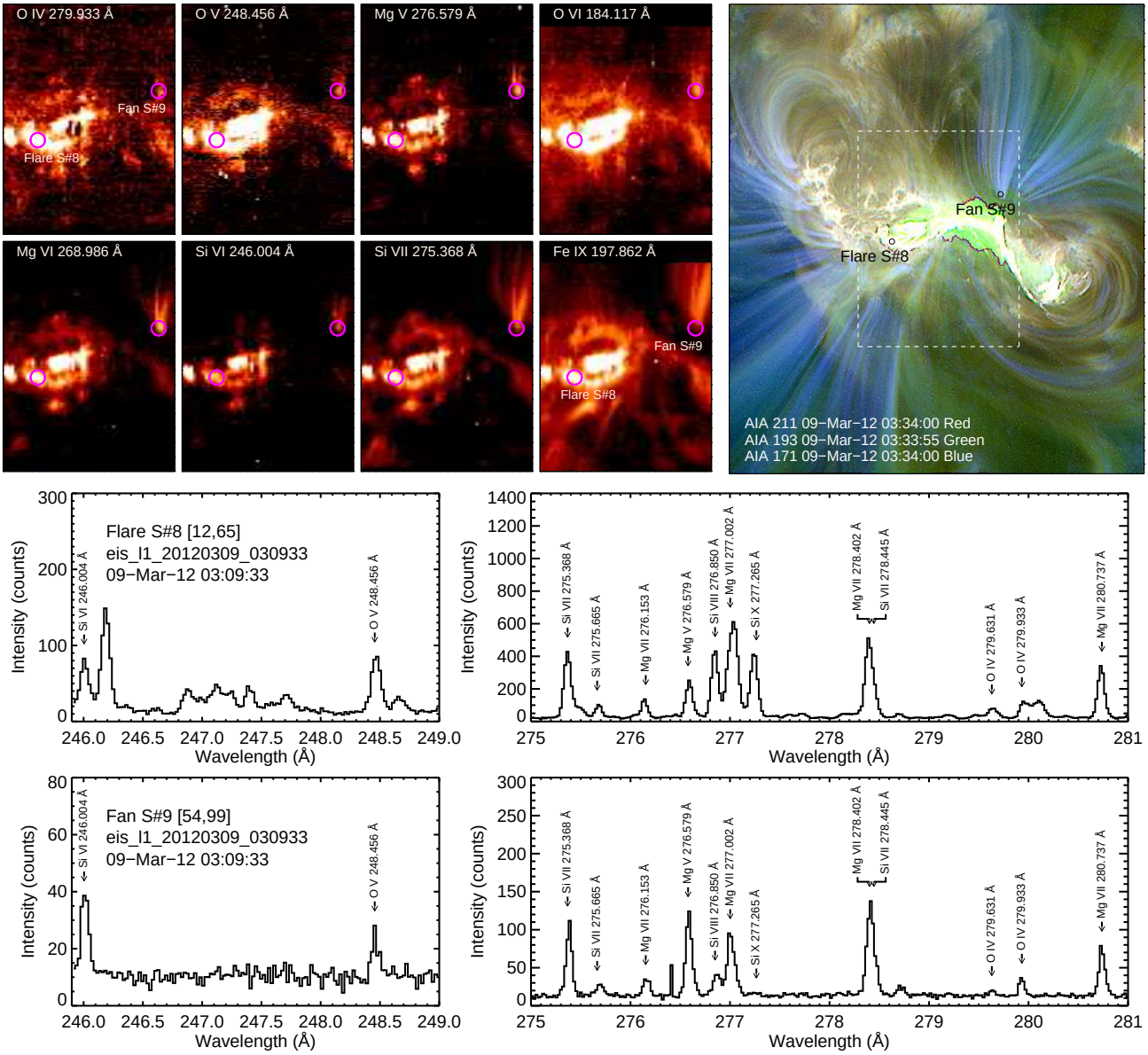


FIG. 5.— EIS and AIA observations of a flaring active region taken on 2012 March 9 between 03:09:33 and 03:40:42 UT. The format is the same as Figure 2.

is comparable to or larger than that of Si VI 246.004 Å and O IV 279.933 Å is generally as bright or brighter than Mg V 276.579 Å.

The spectra suggest that there are systematic differences in the composition of the transient events relative to the long-lived coronal fans. To put this idea on a more secure footing, however, we must account for density and temperature effects.

As mentioned previously, almost all of the emission lines given in Table 1 have some degree of sensitivity to density. The emissivity of O V 248.456 Å, for example, falls by about 25% between $\log n = 10$ and $\log n = 11$. To account for these effects we use the observed Fe XIII 203.826/202.044 Å and Mg VII 280.737/276.153 Å line ratios to infer the electron density. We assume that this emission is formed at the peak temperature of formation and convert these measurements to a total pressure. The pressures derived from these diagnostics are generally consistent to within a factor of two of each other, and we average them to arrive at a pressure for computing the emissivities for each line of interest in each spectrum. These measurements also follow our intuition that the pressure should be higher in strongly heated flare loops than in the fans. In the 2012 March 9 observations, for example, the pressure for the flare spectrum is derived to be $\log P = 16.8$ while the pressure in the fan is observed to be $\log P = 15.9$.

To investigate the temperature structure of the observed plasma we plot the emission measure (EM) loci curve for each line defined by

$$EM(T_e) = \frac{4\pi I_{obs}}{\epsilon_\lambda(T_e, n_e)}, \quad (1)$$

where I_{obs} is the observed intensity and $\epsilon_\lambda(T_e, n_e)$ is the emissivity computed at a constant pressure. We carry out these calculations assuming both photospheric abundances (Caffau et al. 2011) and our approximation to the Feldman et al. (1992) abundances which have the low-FIP elements enriched by a factor of 4 and the value for the high-FIP ele-

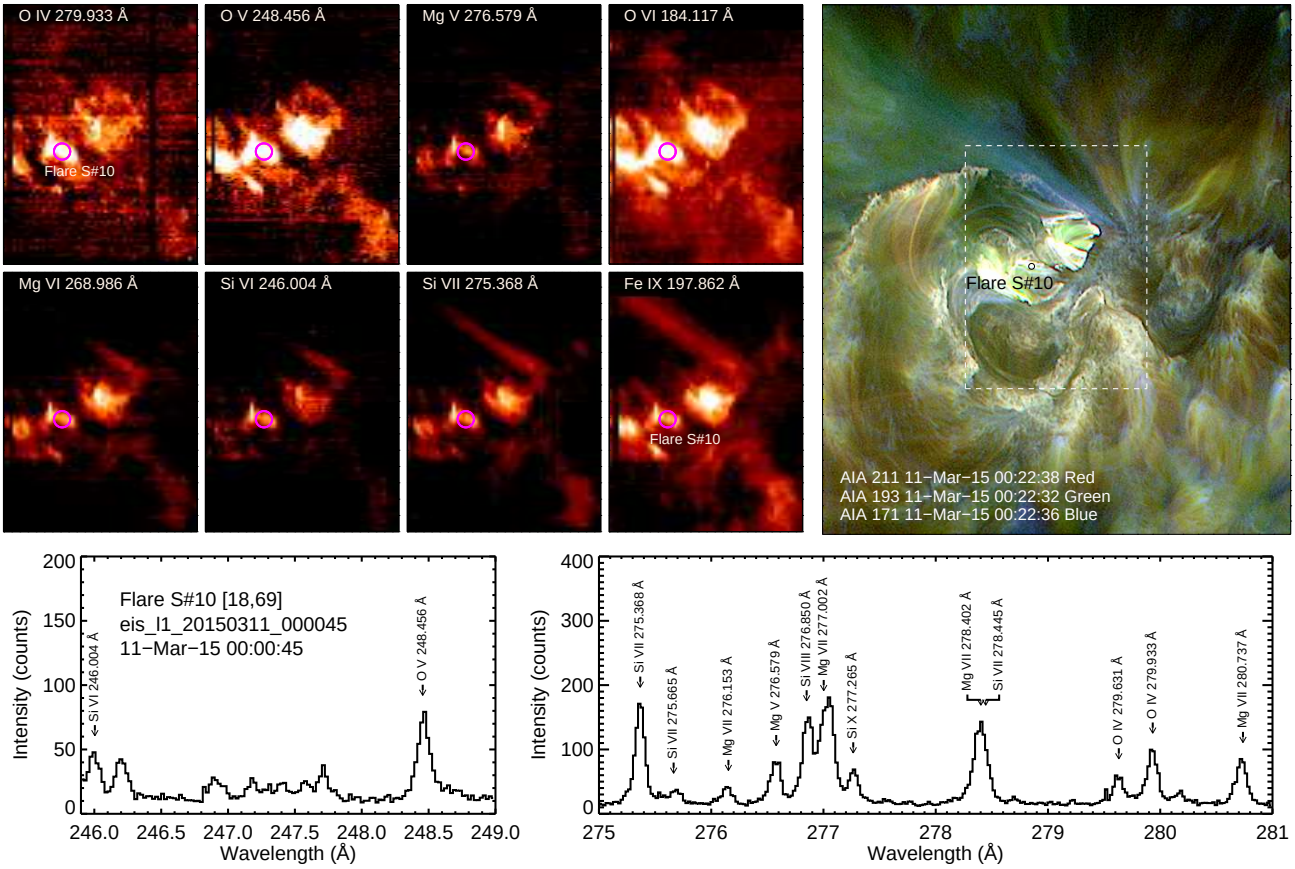


FIG. 6.— EIS and AIA observations of a flaring active region taken on 2015 March 11 between 00:00:45 and 00:31:54 UT. The format is the same as Figure 2.

ments left at their photospheric values. The EM loci curves can be interpreted as an approximate envelope to the differential emission measure distribution, which is the best-fit solution to the ill-posed integral equation,

$$I_{obs} = \frac{1}{4\pi} \int \epsilon_\lambda(T_e, n_e) \xi(T_e)\, dT_e. \qquad (2)$$

It is important to note that an EM loci curve forms an upper bound to the emission measure that can explain the observed intensity. If one emission measure loci curve lies systematically above another, then the intensities of both lines cannot be described by the same emission measure distribution.

Emission measure loci plots for many of the observations are shown in Figures 9 and 10. These plots are consistent with the simple inspection of the spectra. In Figure 9 we show the EM loci for all of the observations of the fans. For each case we see that the observed intensities for the low- and high-FIP elements are more consistent with a coronal composition than with a photospheric one. In each case the intensities of the O lines cannot be reconciled with the intensities of the Mg V and Mg VI lines assuming a photospheric composition.

The EM loci plots for the transient heating events show the opposite trend. For these spectra we see that the intensities for the low- and high-FIP elements are more consistent with a photospheric composition than with a coronal one. In these cases the intensities of the O lines cannot be reconciled with the intensities of the Mg V and Mg VI lines assuming a coronal composition.

As a check on these trends we have also included EM loci curves for the S X 264.233 Å line. S has an FIP of 10.4 eV and sits on the boundary between low- and high-FIP elements. Nevertheless, it has proven to be a useful diagnostic in studies of coronal outflows (e.g, Brooks et al. 2015; Brooks & Warren 2011) and in active regions (e.g., Baker et al. 2015; Del Zanna 2013b). The observations of this coronal line are generally consistent with the interpretation of the transition region emission. The EM loci for S X is generally closer to those of the coronal Fe and Si lines assuming a coronal composition for the fans. For the transient heating events the observed S emission is generally more consistent with a photospheric composition, although there are some exceptions. We show EM loci plots for only 4 of the 8 spectra for the transient heating events. The remaining plots are very similar to what is displayed here.

As a final check on the interpretation of the spectra we have computed differential emission measure distributions for each spectrum assuming both coronal and photospheric abundances for the emissivities. We used the Monte Carlo Markov Chain (MCMC) emission measure algorithm (Kashyap & Drake 1998, 2000) distributed with the `PINTofALE` spectral analysis package to solve Equation 2. This algorithm has the advantage of not assuming a functional form for the differential emission measure. The MCMC algorithm also provides for estimates of the error in the EM by calculating the emission measure using perturbed values for the intensities. These calculations are also consistent with our interpretation of the spectra and the EM loci curves. Again, for the fans the assumption of coronal abundances leads to smaller χ^2 values for the modeled intensities. For the heating events the assumption of photospheric abundances leads to smaller χ^2 values.

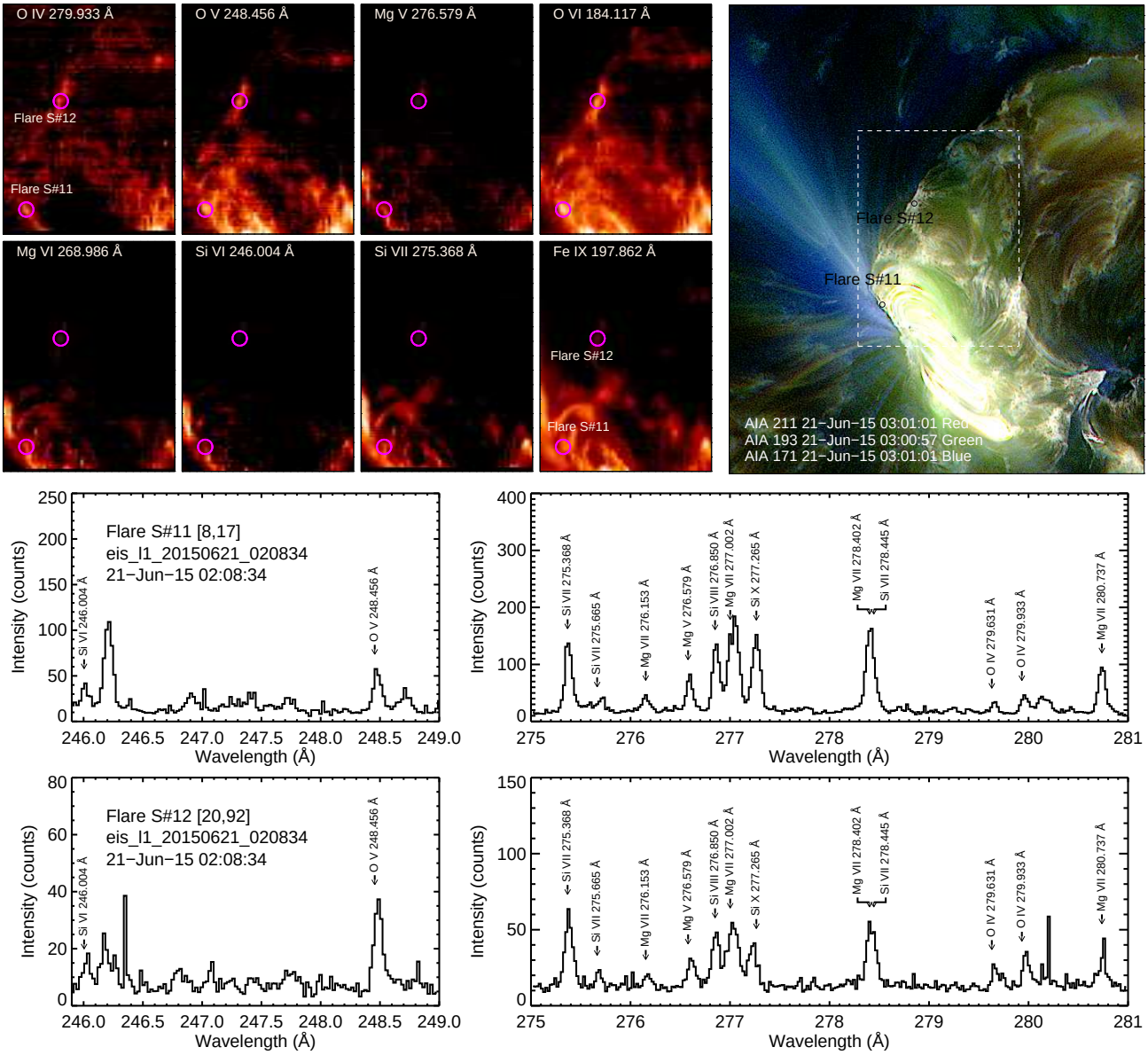


FIG. 7.— EIS and AIA observations of a flaring active region taken on 2015 June 21 between 02:08:34 and 03:09:14 UT. The format is the same as Figure 2.

The DEM calculations also point to the limitations of the EIS data for exploring this issue. For example, since there is no low-FIP line that has good overlap in temperature with O IV the DEM can be adjusted to match its observed intensity regardless of the assumed abundance. Also, since the emissivity of O VI has been adjusted it is useful to perform the DEM calculation without it. In this case a reasonable fit to the fan observations can be achieved for photospheric abundances if the DEM increases very sharply at around $\log T = 5.5$. For the brightenings O VI plays less of a role in determining the structure of the DEM. In these spectra Mg V forms a lower bound to the DEM that is inconsistent with the observed O IV and O V emission if coronal abundances are assumed. These conclusions are evident from inspection of the EM loci curves and we have chosen not to display the DEM curves.

4. SUMMARY AND DISCUSSION

We have presented the analysis of EIS spectra observed during transient heating events. During these times the observed transition region emission is consistent with a photospheric composition. This is inferred from the strong intensities in O IV–O VI emission lines relative to Mg and Si lines formed at similar temperatures. The relative intensities for these lines in the fan loops are much different. In these locations the Mg and Si lines are strong relative to those from O IV–O VI. These trends are clearly reflected in the emission measure loci plots that describe the temperature structure of the plasma at these locations.

Our analysis suggests that the plasma composition could be an important signature of the coronal heating process. Plasma that is evaporated from the chromosphere by strong, impulsive heating, such as in a flare or jet may not show any enrichment in low-FIP elements. Coronal abundances may be a feature of plasma confined to long-lived structures, such as in the fan loops or the high-temperature emission in active region cores.

It is interesting to interpret these results in the context of abundance measurements at transition region temperatures in

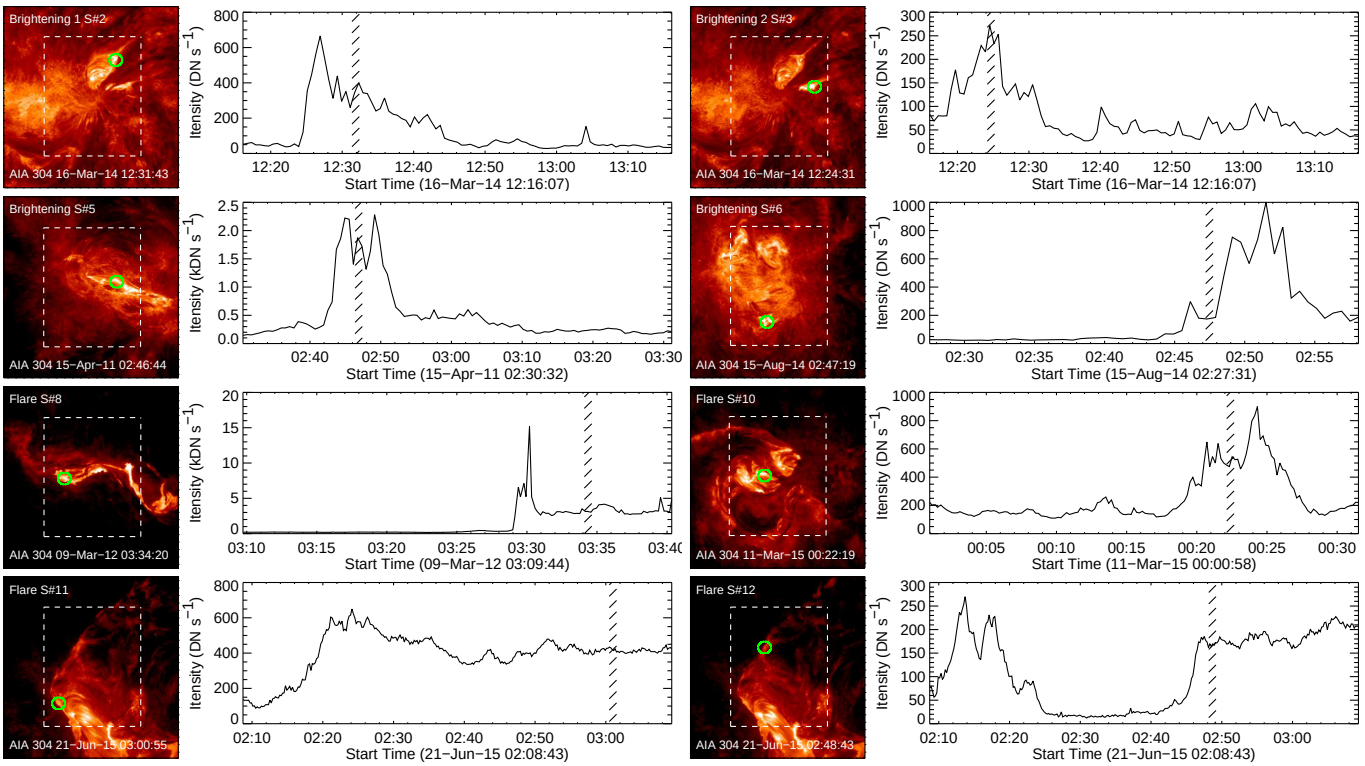


FIG. 8.— AIA 304 Å intensities as a function of time for the transient heating events. The left panels show the AIA 304 Å image at the time of the EIS spectrum that has been analyzed. The position of the EIS observation is indicated by the green circle. The dashed line shows the field of view for the EIS raster. The hashed area on the light curve indicates the time for the EIS spectrum at this position. Note that the vertical scale on some of the light curve plots is 10^3 DN s^{-1}. The light curves for the fans, which are not shown, are approximately constant in time.

the quiet Sun. Analysis by Laming et al. (1995) and Young (2005) have indicated that the FIP effect is greatly reduced or even absent in the quiet Sun at transition region temperatures. In Appendix B we present some EIS quiet Sun spectra which also show a strong reduction in the FIP effect at transition region temperatures. These observations could be consistent with the idea that transition region emission is dominated by short-lived structures, the unresolved fine structures of Feldman (1983), for which the abundances are predominately photospheric.

Unfortunately, a direct connection between the coronal heating process and abundance variations is only a conjecture at this point. More analysis is needed to fully understand how the composition varies from feature to feature and with time. Ideal observations would include many low- and high-FIP emission lines, very high spatial resolution, and high cadence. The Interface Region Imaging Spectrograph (IRIS, De Pontieu et al. 2014) can achieve the high spatial resolution and cadence needed to study the morphology and dynamics of transition region structures. Hansteen et al. (2014), for example, have used IRIS observations to find evidence for highly variable, low lying loops at transition region temperatures. It is not clear, however, that IRIS observes enough low and high-FIP emission lines to infer the plasma composition for these structures. It is possible that coordinated observations between IRIS and EIS will provide useful information, but the mismatch in spatial resolution could be difficult to overcome. Progress on understanding abundance variations and their connection to coronal heating may need to wait for future instrumentation, such as the Marshall Grazing Incidence X-ray Spectrograph (MaGIXS, Kobayashi et al. 2011) or the EUV spectrograph proposed for *Solar-C* (Teriaca et al. 2012).

Hinode is a Japanese mission developed and launched by ISAS/JAXA, with NAOJ as domestic partner and NASA and STFC (UK) as international partners. It is operated by these agencies in co-operation with ESA and NSC (Norway). The authors would like to acknowledge many helpful conversations on this work with Peter Young. The authors would also like to thank Remy Freire, who helped develop the EIS-AIA co-alignment software and began the analysis of several of these events during a summer internship at NRL. This work has been sponsored by NASA's *Hinode* project.

APPENDIX

O VI INTENSITIES IN THE QUIET SUN

In this section we discuss the intensity of the O VI 184.117 Å line. Observations from O VI are needed to improve the overlap between the low- and high-FIP lines in the EIS spectra. In our analysis we have scaled it by a factor of 3.4 to bring it into agreement with the other emission lines formed at similar temperatures. Here we discuss the supporting evidence for this adjustment.

One way to examine the relative consistency of spectral data is to consider observations from the quiet Sun above the limb. Numerous observations have shown that the off-limb, quiet corona has a very narrow temperature distribution (e.g., Raymond et al. 1997; Feldman et al. 1998; Landi et al. 2002; Warren & Brooks 2009). This makes it easy to identify possible inconsistencies between the atomic data and the observed intensities.

To illustrate this type of analysis we use the 2007 November 4 off-limb observations presented by Warren et al. (2014).

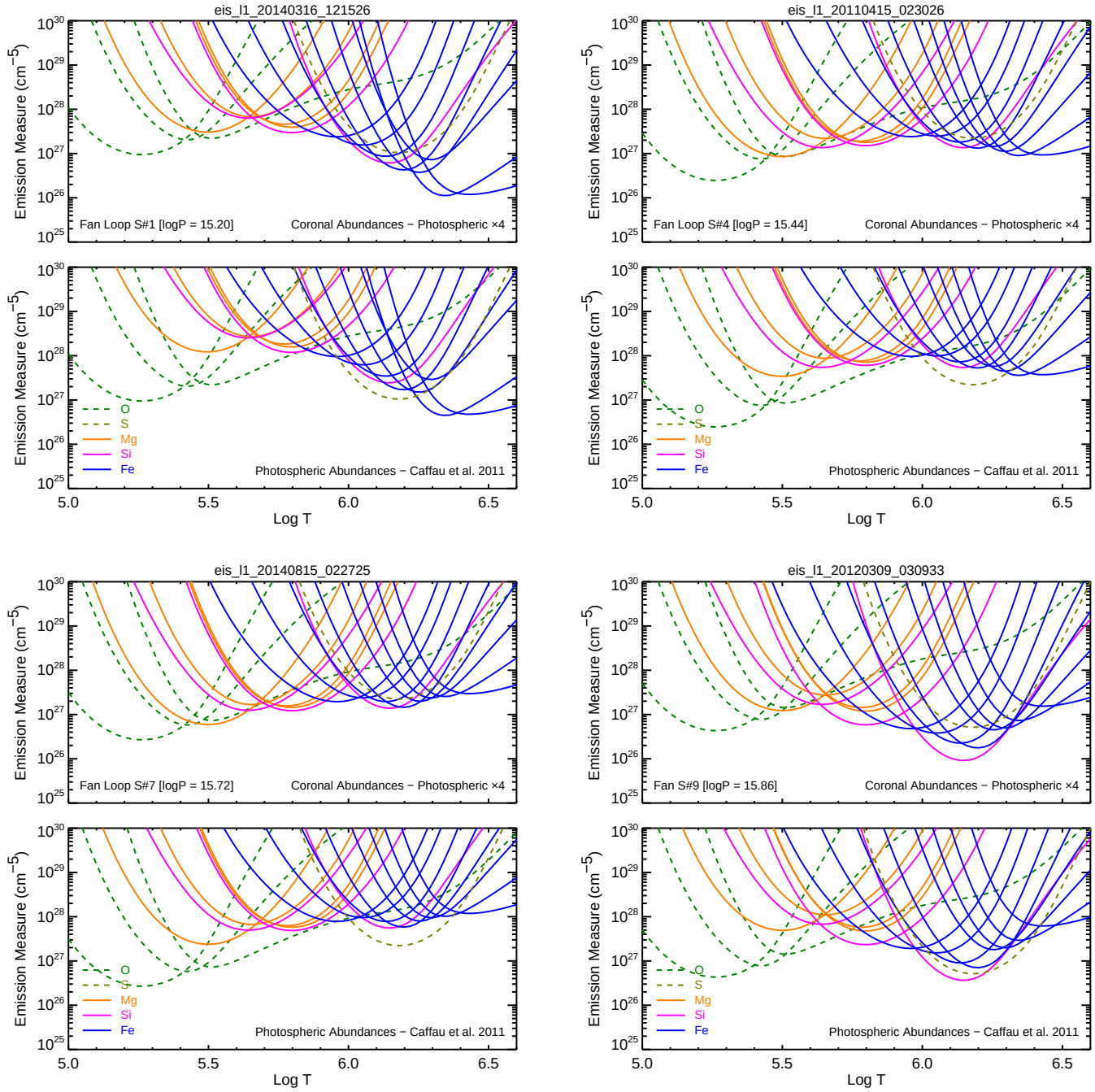


FIG. 9.— Emission measure loci curves for the four fan observations. For each observation calculations for both photospheric and coronal abundances are shown. The observed intensities of the transition region O and Mg lines are more consistent with a coronal composition. The pressure derived from the Fe XIII and Mg VII densities are indicated on each set of plots.

These spectra were formed by averaging about 38 300 s exposures together. The observed intensities for the lines relevant to our study are shown in Table 2. These intensities use the adjusted calibration of Warren et al. (2014). In Figure 11 we show the emission measure loci and differential emission measure distribution derived from these intensities. The Fe and Si lines from ions formed relatively near $\log T = 6.1$ all intersect close to a point, suggesting nearly isothermal plasma. The DEM is also relatively narrow with a Gaussian width of about 10^5 K. Here we have assumed that the DEM is Gaussian in shape. A similar result is obtained using MCMC. When compared with the other lines used in this analysis, the intensity of O VI 184.117 Å is too high by a factor of about 3.4. This is indicated by the EM loci curves shown in Figure 11.

Some previous studies have identified problems in the analysis of the emission from Li-like ions such as O VI (e.g., Dupree 1972; Warren 2005). However, many previous analyses of off limb spectra have successfully used the longer wavelength O VI lines to measure the composition of the corona (e.g., Feldman et al. 1998). Muglach et al. (2010) compared the long wavelength O VI lines observed with SUMER and

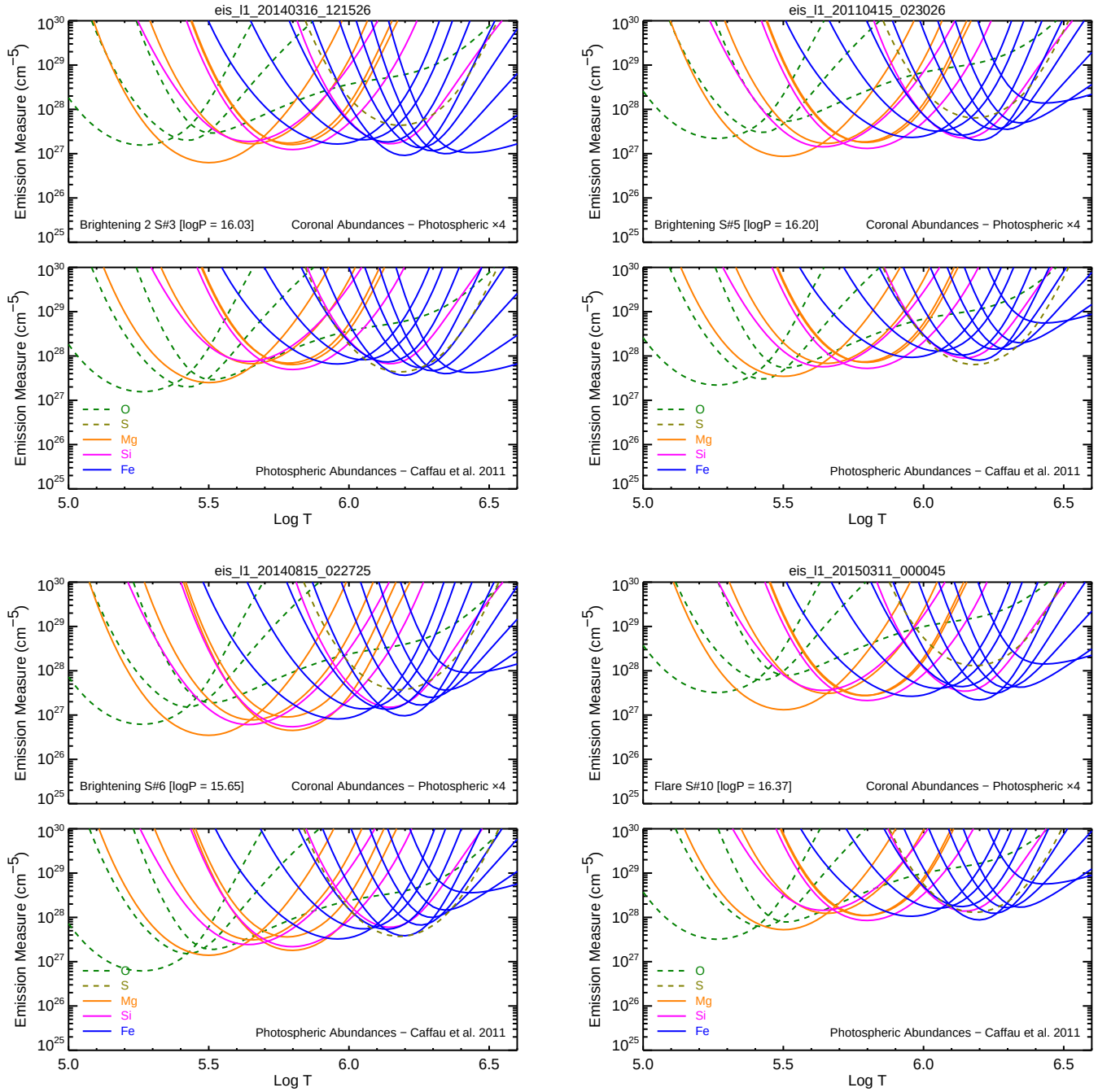


FIG. 10.— Emission measure loci curves for four of the transient heating events. The format is the same as Figure 9. For these features the observed intensities of the transition region O and Mg lines are more consistent with a photospheric composition. The emission measure loci for the other events are similar to these.

the short wavelength O VI lines observed with EIS and found that their intensities could not be reconciled.

O VI peaks at about $\log T = 5.6$ and emission from this ion is observed in the corona because of the long tail on the ionization fraction. In the transient brightenings and flares that we observe we expect the emission from O VI to be formed much closer to the peak in the ionization fraction. We now turn to observations in the quiet Sun, where this also expected to be true.

The intensities of coronal emission lines in the on-disk, quiet Sun have been studied by Brooks et al. (2009), who analyzed 45 full CCD observations taken during the 2007, solar minimum between solar cycles 23 and 24. This analysis provided insights into the temperature structure of the quiet corona and identified which emission lines and atomic data provided consistent results. It did not, however, consider emission at transition region temperatures, which is very weak in the quiet Sun.

We have taken several of the observations from the Brooks et al. (2009) study and constructed spatially and temporally averaged spectra. These spectra cover a region $90'' \times 90''$ in area with the $1''$ slit and $1''$ steps. Each exposure was 90 s in duration. This accumulates to about 7.3×10^5 s of observing. Two of these quiet Sun spectra are shown in Figure 12.

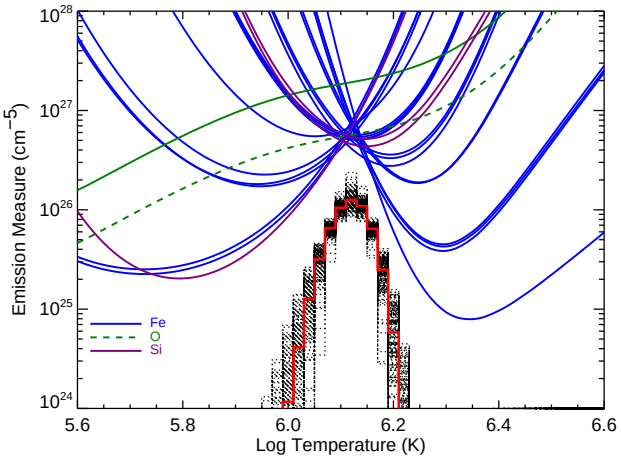


FIG. 11.— The emission measure for the quiet Sun, off-limb observations. The red line is the differential emission measure as a function of temperature. Emission measure loci curves are shown for the lines given in Table 2. The EM loci for O VI 184.117 Å is shown scaled (green dash) and unscaled (green solid).

TABLE 2
MODELING EIS OFF-LIMB OBSERVATIONS[a]

Line	I_{obs}	I_{dem}	R
Fe VIII 185.213	21.30	21.92	1.0
Fe VIII 186.601	17.45	16.08	1.1
Si VII 275.368	8.39	8.96	0.9
Fe IX 188.497	37.57	41.87	0.9
Fe IX 189.941	19.13	19.09	1.0
Fe IX 197.862	23.97	21.97	1.1
Fe X 184.536	256.62	198.67	1.3
Fe XI 180.401	948.90	892.12	1.1
Fe XI 188.216	422.43	424.65	1.0
Fe XI 188.299	291.92	261.12	1.1
Fe XI 192.813	90.06	89.19	1.0
Fe XII 192.394	141.05	150.80	0.9
Fe XII 193.509	323.34	318.25	1.0
Fe XII 195.119	367.57	470.87	0.8
Si X 258.375	126.01	119.50	1.1
Si X 261.058	68.07	76.63	0.9
Fe XIII 202.044	236.04	186.15	1.3
Fe XIII 203.826	44.11	37.34	1.2
Fe XIV 211.316	37.02	35.94	1.0
Fe XIV 270.519	8.04	8.93	0.9
Fe XIV 274.203	21.33	20.36	1.0
Fe XV 284.160	17.20	17.25	1.0
O VI 184.117	9.01	8.83	1.0

[a] Observed intensities are from 2007 November 4 and use the Warren et al. (2014) effective areas. The computed intensities are from the Gaussian DEM and R is the ratio of observed to computed. The O VI line uses the scaled emissivity. The units for the intensities are erg cm^2 s^{-1} sr^{-1}.

Inspection of the averaged spectra indicate that the relative line intensities are similar to what is observed in the transient heating events. The high-FIP O lines are strong relative to the low-FIP Si and Mg lines.

We have fit all of the relevant lines with Gaussians and computed calibrated line intensities. The Fe XIII and Mg VII ratios are used to compute electrons densities and total pressures, which are much smaller than those observed in the active regions. The EM loci curves are shown in Figure 13 and are consistent with the simple inspection of the spectra. The EM loci computed assuming photospheric abundances are more consistent than those computed assuming a coronal composition. Even for photospheric abundances, however, there is an offset between the O and Mg lines. The Mg lines are very weak and it difficult to assess the uncertainties in the intensities.

The EM loci for O VI using both the computed emissivity from CHIANTI and the scaled emissivity are shown in Figure 13. It is clear from these plots that without the application of some sort of adjustment the O VI 184.117 Å line is not in agreement with the other O lines or the Mg and Si lines. Scaling the emissivity for this line by a factor of 3.4 makes it more consistent with the EM loci curves for the other O lines.

APPENDIX

THE EIS CALIBRATION

The relative calibration of EIS is an important component of this analysis. Del Zanna (2013b) noted that some temperature and density insensitive line ratios that involved the long and short wavelength detectors were not in agreement with theory. The Fe XXIV 192.04/255.10 Å ratio, for example, should be 2.5 but was observed to be above 4 and changing with time. Del Zanna (2013b) and Warren et al. (2014) proposed modifications to the pre-flight calibration that attempted to reconcile the available atomic data and the observations. Warren et al. (2014) fit the time-dependent trends in the effective areas with exponentials, which allows them to be extrapolated to the more recent observations that we have analyzed here.

We have fit the Fe XXIV lines in each spatial pixel for both the 2015 June 21 and 2015 March 11 observations. Taking care to avoid spectra for which the 192.04 Å line is saturated, we find median ratios of 2.61 and 2.51 using the revised calibration, which is in agreement with theory. The pre-flight calibration yields ratios of 4.8 and 4.7.

A similar analysis of the Fe XIV 274.203/211.316 Å branching ratio in these observations yields less satisfactory results. The theoretical ratio from CHIANTI is 0.52. Using the pre-flight calibration we obtain ratios of 0.19 and 0.18. Applying the revised calibration yields ratios of 0.78 and 0.79, which are about 50% too high. Inspection of the EM loci curves for the recent observations presented in Figures 2–7 indicates generally good agreement between the long and short wavelength lines. For example, Si VII 275.368 and Si X 258.375 Å are generally in good agreement with the Fe lines formed at similar temperatures. This suggests that the evolution of the EIS effective area near 211 Å is not being properly accounted for in the revised calibration. Additional work is underway to evaluate and correct this problem.

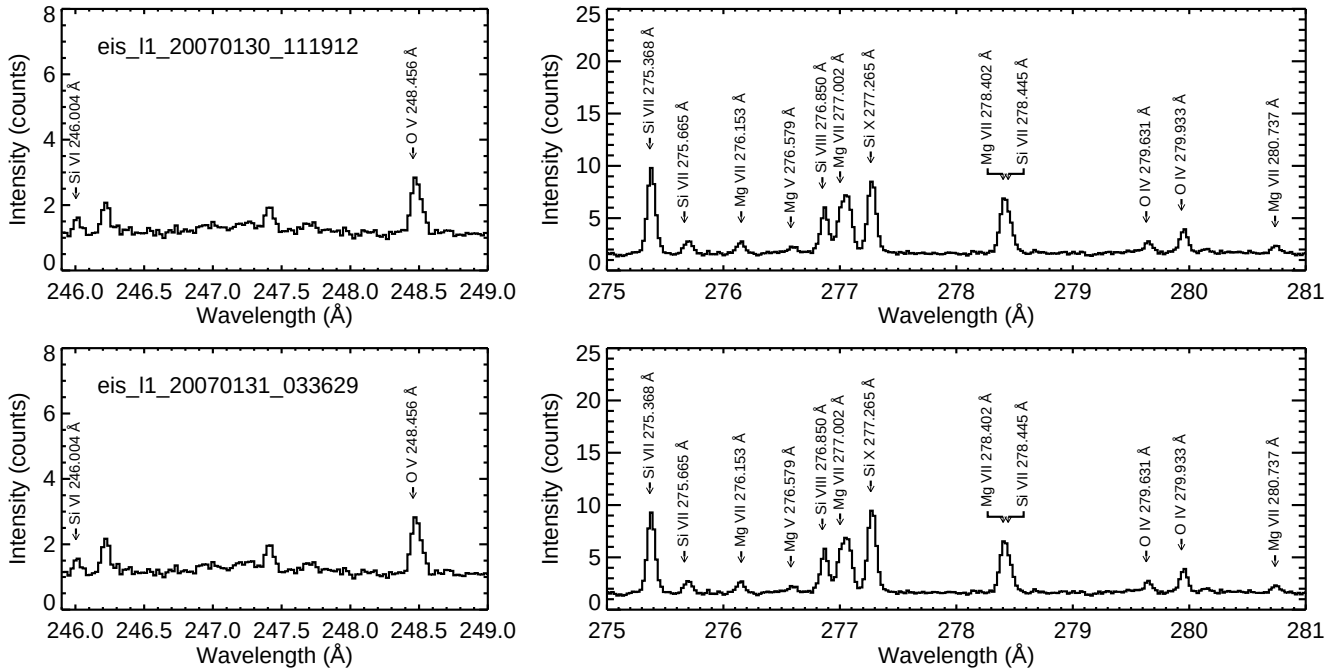


FIG. 12.— Spatially and temporally averaged EIS spectra from on-disk, quiet Sun observations. These spectra show that the high-FIP O lines are strong relative to the low-FIP Mg and Si lines, suggesting a composition close to that of the photosphere for transition region emission in the quiet Sun.

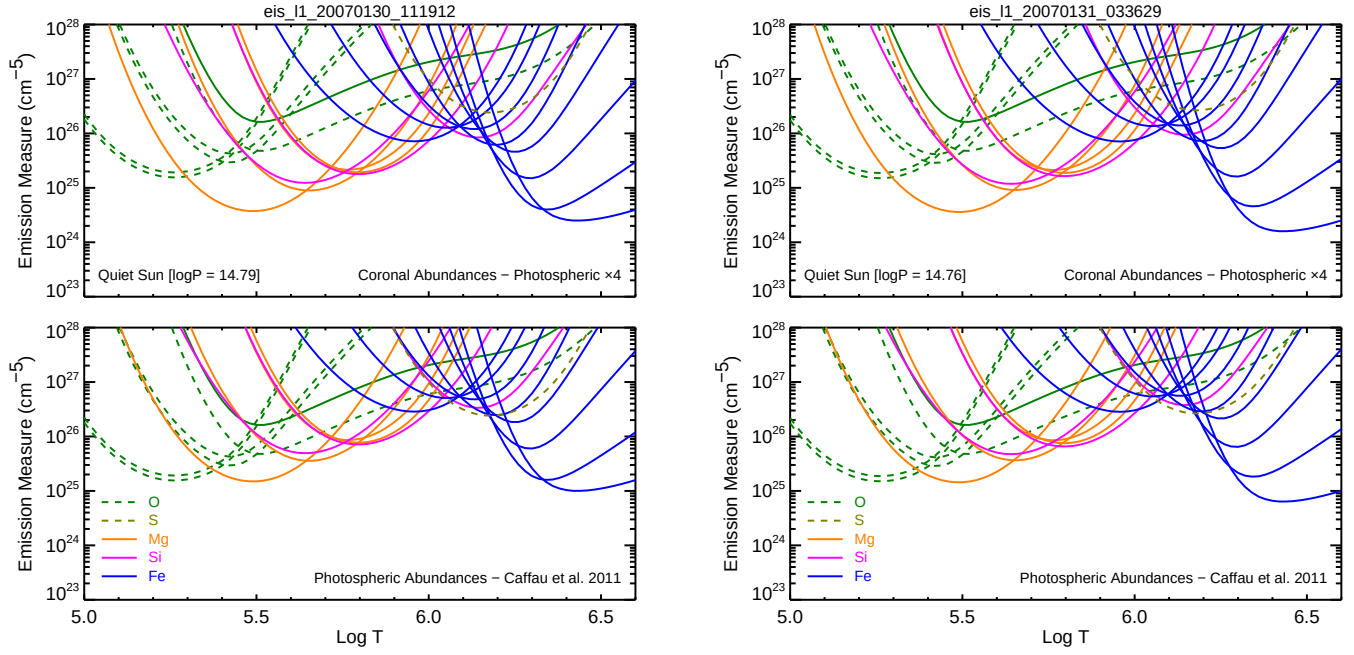


FIG. 13.— Emission measure loci curves for the on-disk, quiet Sun spectra shown in Figure 12. The format is the same as Figures 9 and 10. The quiet Sun intensities appear to be more consistent with photospheric abundances than with coronal abundances. In either case the O VI 184.117 Å line is discrepant. Multiplying it by the factor of 3.4 derived from the off-limb spectra brings it into closer agreement with the other O lines. the solid green line is the emissivity as calculated from CHIANTI.

REFERENCES

Baker, D., Brooks, D. H., Démoulin, P., et al. 2015, ApJ, 802, 104
Brooks, D. H., Ugarte-Urra, I., & Warren, H. P. 2015, Nature Communications, 6, 5947
Brooks, D. H., & Warren, H. P. 2011, ApJ, 727, L13
Brooks, D. H., Warren, H. P., Williams, D. R., & Watanabe, T. 2009, ApJ, 705, 1522
Caffau, E., Ludwig, H.-G., Steffen, M., Freytag, B., & Bonifacio, P. 2011, Sol. Phys., 268, 255
Culhane, J. L., Harra, L. K., James, A. M., et al. 2007, Sol. Phys., 243, 19
De Pontieu, B., Title, A. M., Lemen, J. R., et al. 2014, Sol. Phys., 289, 2733
Del Zanna, G. 2013a, A&A, 555, A47
—. 2013b, A&A, 558, A73
Del Zanna, G., Dere, K. P., Young, P. R., Landi, E., & Mason, H. E. 2015, A&A, 582, A56
Del Zanna, G., & Mason, H. E. 2014, A&A, 565, A14
Dennis, B. R., Phillips, K. J. H., Schwartz, R. A., et al. 2015, ApJ, 803, 67
Dere, K. P., Landi, E., Mason, H. E., Monsignori Fossi, B. C., & Young, P. R. 1997, A&AS, 125, 149
Doschek, G. A., Warren, H. P., & Feldman, U. 2015, ApJ, 808, L7
Dupree, A. K. 1972, ApJ, 178, 527
Feldman, U. 1983, ApJ, 275, 367
Feldman, U., Mandelbaum, P., Seely, J. F., Doschek, G. A., & Gursky, H. 1992, ApJS, 81, 387
Feldman, U., Schühle, U., Widing, K. G., & Laming, J. M. 1998, ApJ, 505, 999
Fludra, A., & Schmelz, J. T. 1999, A&A, 348, 286
Freeland, S. L., & Handy, B. N. 1998, Sol. Phys., 182, 497
Hansteen, V., De Pontieu, B., Carlsson, M., et al. 2014, Science, 346, arXiv:1412.3611
Kashyap, V., & Drake, J. J. 1998, ApJ, 503, 450
—. 2000, Bulletin of the Astronomical Society of India, 28, 475
Kobayashi, K., Cirtain, J., Golub, L., et al. 2011, in Society of Photo-Optical Instrumentation Engineers (SPIE) Conference Series, Vol. 8147, Society of Photo-Optical Instrumentation Engineers (SPIE) Conference Series, 1
Korendyke, C. M., Brown, C. M., Thomas, R. J., et al. 2006, Appl. Opt., 45, 8674
Laming, J. M. 2015, Living Reviews in Solar Physics, 12, 2
Laming, J. M., Drake, J. J., & Widing, K. G. 1995, ApJ, 443, 416
Landi, E., Feldman, U., & Dere, K. P. 2002, ApJ, 574, 495
Landi, E., & Young, P. R. 2009, ApJ, 706, 1
Lang, J., Kent, B. J., Paustian, W., et al. 2006, Appl. Opt., 45, 8689
Muglach, K., Landi, E., & Doschek, G. A. 2010, ApJ, 708, 550
Raymond, J. C., Kohl, J. L., Noci, G., et al. 1997, Sol. Phys., 175, 645
Sheeley, Jr., N. R. 1995, ApJ, 440, 884
Sylwester, B., Phillips, K. J. H., Sylwester, J., & Kępa, A. 2015, ApJ, 805, 49
Teriaca, L., Andretta, V., Auchère, F., et al. 2012, Experimental Astronomy, 34, 273
Warren, H. P. 2005, ApJS, 157, 147
—. 2014, ApJ, 786, L2
Warren, H. P., & Brooks, D. H. 2009, ApJ, 700, 762
Warren, H. P., Ugarte-Urra, I., & Landi, E. 2014, ApJS, 213, 11
Warren, H. P., Winebarger, A. R., & Brooks, D. H. 2010, ApJ, 711, 228
—. 2012, ApJ, 759, 141
Widing, K. G., & Feldman, U. 2001, ApJ, 555, 426
Young, P. R. 2005, A&A, 444, L45